NUMERICAL AND EXPERIMENTAL ANALYSIS OF EMI-INDUCED NOISE IN RC PHASE SHIFT OSCILLATOR

H.-C. Tsai[*]

Department of Electronic Engineering, Chen-Shiu University, No. 840, Chengcing Road, Neausong District, Kaohsiung 83305, Taiwan

Abstract—Electromagnetic interference (EMI) has an adverse effect on the performance of electronic circuit communication systems. This study derives a series of equations to analyze the effects of the EMI induced in a conducting wire on the noise spectrum of a RC Phase Shift Oscillator (RCPSO). It is shown that the extent to which EMI affects the RCPSO depends on the interference power, interference frequency, induced power, output resistance of oscillator circuit, and parasitic capacitance. Specifically, higher EMI frequencies and amplitudes have a greater effect on the RCPSO output. The results presented in this study are in good agreement with those predicted from general EMI theory.

1. INTRODUCTION

For many nations, the state of the domestic electronics industry provides a good indicator of the nation's general economic wellbeing. Thus, the manufacture of electronic components is a central element in the development plans of many governments around the world. With the proliferation of wireless and electronic devices in recent years, the environment is becoming increasingly saturated with electromagnetic waves. Whilst some of these waves, termed as "signals", are necessary and useful in that they fulfill a specific design purpose, others are undesirable since they interfere with nearby electrical or electronic devices. For example, a cell phone used next to a computer may cause a distortion of the image on the screen or a static blast

from the speakers. Thus, when designing electronic components, the aim is to develop high quality products which perform reliably in electromagnetic interference (EMI) contaminated environments without interfering with neighboring devices themselves.

The literature contains a large number of studies on the mitigation of EMI effects [1–15]. For example, in [2], a method was proposed for detecting EMI-induced errors in radio frequency integrated circuit (RFIC) autotest-equipment (ATE) and for recovering these errors via a retest procedure. In a recent study [6], it was shown that external EMI can still interfere with shielded active circuits at certain frequencies of the interference source. In [9], the authors presented a new method for calibrating non-stationary electromagnetic field measurements based on the double modulation of a standard exciting source. In power substations, the EMI generated during the switching of disconnectors and circuit breakers can cause nearby electronic equipment to malfunction or fail if it is not adequately shielded. Consequently, the authors in [10] performed a finite element analysis of three common shielding and filtering methods, namely metallic channel, braided cable and additional cable. In [10], the authors examined two un-resolved problems in the high-tech industry field, namely the interpretation of EMI laboratory correlation studies and the margin below the CISPR 22 limit at which EMI compatibility compliance can still be achieved.

However, modern electrical circuits comprise an ever increasing number of electronic components packaged within devices of ever reducing size. The high transmission speeds and operating frequencies of these circuits, combined with an increasing wiring density, not only increase the risk of the circuit interfering with other electronic devices, but also increase the susceptibility of the device to EMI. As a result, it is essential that the effects of EMI on common electronic components are thoroughly understood such that appropriate mitigating measures can be taken.

Accordingly, this study examines the effect of EMI on the noise spectrum of an RC Phase Shift Oscillator (RCPSO), a wavelength-based device with many applications in the electronics field. In a normal indoor environment, the intensity of the low frequency electromagnetic waves is greater than that of the high frequency waves, i.e., $0.03\,\mu\text{T}$ and $0.0067\,\mu\text{T}$, respectively (as measured by the current authors using CA40/43 instrumentation (Chauvin Arnoux, France)). Therefore, in analyzing the effects of EMI on the RCPSO, the present analysis focuses specifically on low frequency EMI.

2. EXPERIMENTS

Figure 1 shows the experimental setup used to measure the interference noise spectrum of the RCPSO. As shown, a conducting wire (CW) was positioned in the air gap of a ferromagnetic toroid wrapped in a current-carrying coil. During the experiments, an EMI source was simulated by applying a voltage across points A and B of the coil, causing a current to flow in the CW. The resulting magnetic field induced in the air gap was amplified by a 74 dB low-noise pre-amplifier such that it could be detected by an oscilloscope and was then connected in series with the RCPSO circuit. In other words, the EMI interference was detected initially as radiated noise and was then coupled with the RCPSO circuit as conducted noise. The EMI signals induced in the RCPSO were transmitted to the oscilloscope via the circuit coupling and were then passed to a spectrum analyzer to generate the corresponding time domain and frequency spectrum plots. In characterizing the noise spectrum of the RCPSO, the EMI frequency was varied in the range of 300 Hz to 1 kHz while the interference amplitude was varied between 0.3 V and 1.0 V. As shown in Fig. 1, the entire measurement system was shielded in a metal case to minimize the effects of external noise. Furthermore, both the low noise amplifier and the V_{DC} source were battery-powered. Finally, the signal analyzer (model HP E4440A) was controlled by a PC via an IEEE-488 bus.
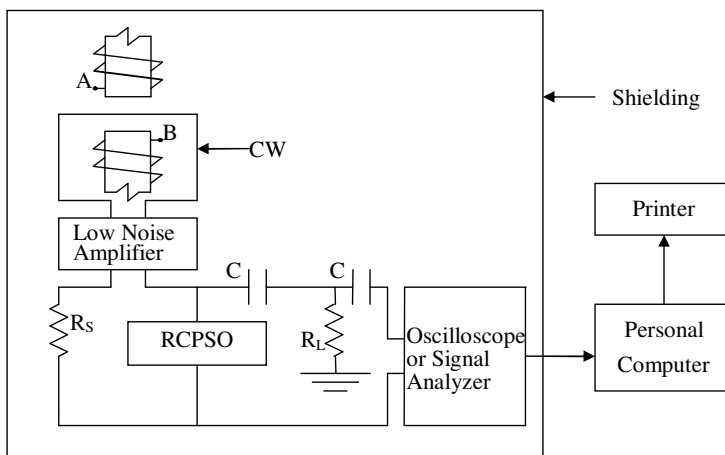

Figure 1. Experimental setup for noise measurement of RCPSO.

3. THEORETICAL ANALYSIS

3.1. Circuit Design

Figure 2 presents the experimental circuit of the RCPSO. In general, two basic types of oscillator exist, namely positive feedback oscillators and negative resistor oscillators. Positive feedback oscillators can be further classified as:

1. Inductance feedback oscillators (e.g., Armstrong oscillators and Hartley oscillators);

2. LC feedback (e.g., Colpitts oscillators);

3. RC feedback (e.g., RC phase shift oscillators);

4. Crystal oscillators.

Oscillators can also be classified in accordance with their output waveforms, i.e.,

1. Non-sinusoidal wave oscillators (e.g., astable multivibrators and blocking oscillators).

2. Sinusoidal wave oscillators (e.g., Wein-bridge oscillators and RC phase shift oscillators).

Finally, the three necessary conditions for oscillation are as follows:

1. Positive feedback;

2. Sufficient amplified gain;

3. Equal feedback voltage phase and input voltage phase.

Figure 3 presents a basic block diagram of the feedback circuit in an oscillator. As shown, the signal V_i is passed through a gain A and is then passed through an attenuator with a feedback factor β and fed back to the input terminal. Assuming that Fig. 3 shows a positive
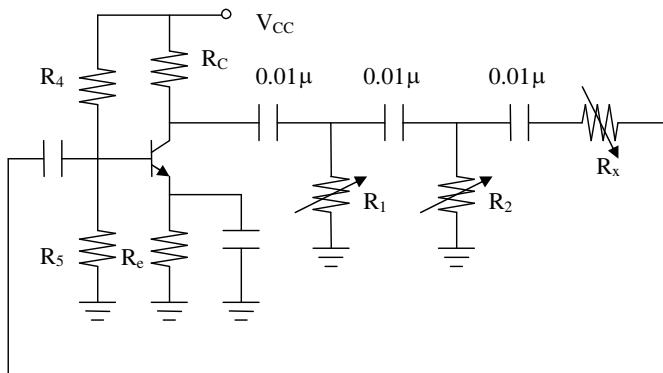

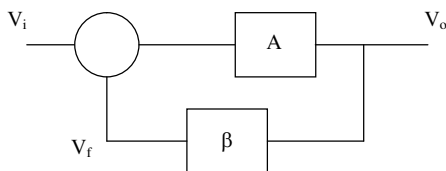**Figure 2.** Experimental circuit of RCPSO.

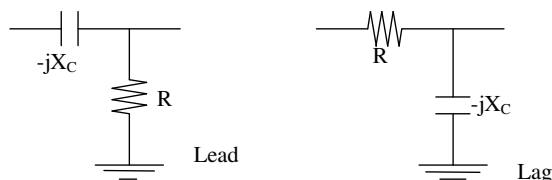**Figure 3.** Basic feedback circuit of oscillator.

Figure 4. Basic circuit diagrams of phase-lead and phase-lag RCPSOs.

feedback mechanism, the output voltage is given by

$$V_o = (V_i + V_f)\,A = (V_i + \beta V_o)\,A = AV_i + A\beta V_o$$

$$V_o(1 - \beta A) = AV_i \Rightarrow V_o = \frac{A}{1 - \beta A}V_i \tag{1}$$

If $\beta A \cong 1$, V_o becomes infinite. This condition is clearly undesirable since it results in a distortion of the waveform.

If V_i is disconnected, then $V_o = \beta A V_o$. For the particular case of $\beta A = 1$, the output voltage has the form of a stable sine wave.

As shown in Fig. 4, RCPSOs can be classified as either phase-lead or phase-lag oscillators.

In the RCPSOs shown in Fig. 4, the phase shift is given by

$$\theta = \tan^{-1} \frac{X_C}{R} \tag{2}$$

Furthermore, the current is obtained as

$$I = \frac{V}{R - jX_C} = \frac{V}{\gamma \angle - \theta} = \frac{V}{\gamma}\angle\theta, \quad V_R = IR = \frac{VR}{\gamma}\angle\theta \tag{3}$$

In general, a total of three RC attenuation circuits connected in series are required to achieve a 180° RC phase shift. The corresponding circuit is shown in Fig. 5.

In Fig. 5, if $R_1 = R_2 = R_3$ and $C_1 = C_2 = C_3$, it follows that $R_C = \frac{1}{SC} = \frac{1}{j\omega C} = \frac{-j}{\omega C} = -jX_C$.
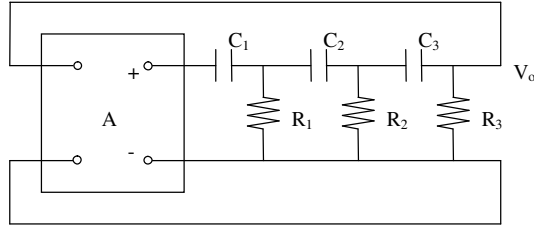
Figure 5. Series arrangement of three RC phase shift circuits.

According to the loop current method in general network theory:

$$V = I_1 (R - jX_C) - I_2 R + I_3 \cdot 0$$
$$0 = -I_1 R + I_2 (2R - jX_C) - I_3 R$$
$$0 = I_1 \cdot 0 - I_2 R + I_3 (2R - jX_C)$$

Thus, it can be shown that

$$I_3 = \frac{\begin{vmatrix} R - jX_C & -R & V \\ -R & 2R - jX_C & 0 \\ 0 & -R & 0 \end{vmatrix}}{\begin{vmatrix} R - jX_C & -R & 0 \\ -R & 2R - jX_C & -R \\ 0 & -R & 2R - jX_C \end{vmatrix}}$$

$$= \frac{VR^2}{(R - jX_C)(2R - jX_C)^2 - [R^2 (R - jX_C)] + [R^2 (2R - jX_C)]}$$

$$= \frac{VR^2}{\left(4R^3 - 8jR^2 X_C - 5jRX_C^2 - jX_C^3\right) - \left(3R^3 - 2jR^2 X_C\right)}$$

$$= \frac{VR^2}{R^3 - 5RX_C^2 - j\left(6R^2 X_C - X_C^3\right)} \tag{4}$$

In the case of a 180° phase difference, the imaginary part of Eq. (4) is equal to zero. Thus, it follows that

$$6R^2 X_C - X_C^3 = 0, \quad X_C \left(6R^2 - X_C^2\right) = 0$$

$$\because X_C \neq 0 \Rightarrow 6R^2 = X_C^2 = \frac{1}{\omega^2 C^2}$$

$$\omega^2 = \frac{1}{6R^2 C^2} \tag{5}$$

$$\omega = \frac{1}{\sqrt{6}RC} = 2\pi f \Rightarrow f = \frac{1}{2\pi \sqrt{6}RC}$$

Substituting Eq. (5) into Eq. (4) gives

$$V_3 = I_3 R = \frac{V R^3}{R^3 - 5 R X_C^2} = \frac{V R^3}{R^3 - 5 R \times 6 R^2} = \frac{V}{-29} = -\frac{1}{29} V \Rightarrow \beta = -\frac{1}{29}$$

Note that the negative sign indicates a 180° phase difference. It follows that the amplifier gain is given by

$$A_V \geq 29 \tag{6}$$

The RCPSO circuit design process can be summarized as follows:

1. Choose R_C and R_{L1}, and obtain γ_L:

If $R_C = 1^k$ and $R_1 = 1^k = R_2 = R_3$, where $R_3 = R_x + R_4//R_5//(\beta\gamma_e') = 1^k$, $R_{L1} = R_1//R_2//R_3 = 333^\Omega$, then $\gamma_L = R_C//R_{L1} = 1^k//333^\Omega = 250^\Omega$.

2. Obtain $\gamma_e'(A_V = \frac{\gamma_L}{\gamma_e})$:

If $A_V = 63$, then $\gamma_e' = \frac{250^\Omega}{63} = 3.97^\Omega$.

3. Determine I_C and I_B and obtain R_e:

$$I_C \cong I_E = \frac{25\,\text{mV}}{\gamma_e'} = \frac{25\,\text{mV}}{3.97^\Omega} = 6.3\,\text{mA}$$

$$I_B = \frac{I_C}{\beta} = \frac{6.3\,\text{mA}}{182} = 0.0346\,\text{mA}$$

If $V_{CC} = 10^V \Rightarrow V_{CE} = V_{CC} - I_C(R_C + R_e) = I_C\gamma_L$

$$I_C = \frac{V_{CC}}{\gamma_L + R_C + R_e} \quad \text{(Design for maximum vibration voltage)}$$

$$6.3\,\text{mA} = \frac{10^V}{250^\Omega + 1^k + R_e}$$

$$R_e = \frac{10^V - 6.3\,\text{mA}\,(1.25^k)}{6.3\,\text{mA}} = 337^\Omega \quad (\text{Assume } R_e = 333^\Omega).$$

4. Determine R_4 and R_5:

Substitute $K = 15$ for R_5

$$R_5 = \frac{V_B}{K I_B} = \frac{0.6^V + 6.3\,\text{mA} \times 0.333^k}{15 \times 0.0346\,\text{mA}} = 5.2^k$$

$$V_B = V_{CC} \times \frac{R_5}{R_4 + R_5} = V_{BE} + I_E R_e \cong V_{BE} + I_C R_e$$

$$R_4 = \frac{V_{CC}}{K I_B} - R_5 = \frac{10^V}{15 \times 0.0346\,\text{mA}} - 5.2^k = 14.07^k.$$

5. Check $\beta R_e \gg R_4//R_5$:

$$\beta R_e = 182 \times 0.333 = 60.606^k \gg 14.07^k//5.2^k$$

6. Determine suitable quiescent operating point:

$$2I_C\gamma_L = 2 \times 6.3\,\text{mA} \times 250^\Omega = 3.15^V$$

$$2V_{CE} = 2\left[V_{CC} - I_C\left(R_C + R_e\right)\right] = 2\left[10^V - 6.3\,\text{mA}\left(1^k + 333^\Omega\right)\right]$$

$$= 3.204^V \cong 3.15^V.$$

Note that the circuit design above is satisfactory since it obtains the suitable quiescent operating point.

3.2. Electromagnetic Interference

In the present study, the interference source has the form of a current-carrying coil wound on a ferromagnetic toroid containing an air gap (Fig. 1). When a current is passed through the coil, an EMI voltage of magnitude V_{eff} is induced in the conducting wire (CW) positioned within the air gap. The magnetic field density and flux density in the air gap are given respectively by [16]

$$H_g = \frac{\mu N I_0}{\mu_0\left(2\pi r_0 - l_g\right) + \mu l_g} \tag{7}$$

$$P_{rB} = \frac{1}{2}\int \mu_0 H_g^2 dv = \frac{1}{2}\int H_g B_g dv \tag{8}$$

where μ_0 is the permeability of free space, μ is the permeability of the ferromagnetic material, I_0 is the current carried by the coil, r_0 is the mean radius of the toroid, and l_g is the width of the air gap.

In general, any periodic signal can be represented by the following complex Fourier series:

$$V(t) = \sum_{n=-\infty}^{\infty} C_n e^{jn\omega t} = C_0 + \sum_{n=1}^{\infty} 2\left|C_n\right|\cos\left(n\omega t + \angle C_n\right) \tag{9}$$

where

$$C_n = \frac{1}{T}\int_{-\frac{T}{2}}^{\frac{T}{2}} V(t)\, e^{jn\omega t} dt \tag{10}$$

In the present experiments, the input signal of the ferromagnetic toroid has the form of the periodic square wave shown in Fig. 6. Thus, the following Fourier transform applies:

$$C_n = \frac{1}{T}\int_0^{t_0} V_0(t)\, e^{-jn\omega t} dt = \frac{V_0 t_0}{T}\frac{\sin\frac{1}{2}n\omega t_0}{\frac{1}{2}n\omega t_0} e^{-j\frac{1}{2}n\omega t_0} \tag{11}$$
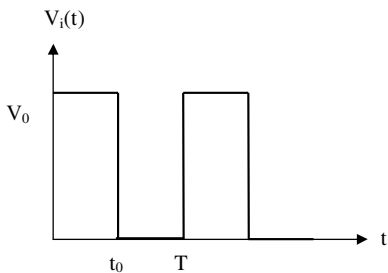
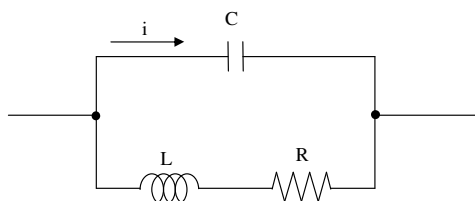**Figure 6.** Input signal of ferromagnetic toroid.

Figure 7. Equivalent circuit of ferromagnetic toroid.

and

$$K_n = \frac{V_0 t_0}{T} \frac{\sin \frac{1}{2} n\omega t_0}{\frac{1}{2} n\omega t_0} \tag{12}$$

$$\angle C_n = \frac{1}{2} n\omega t_0 \tag{13}$$

Substituting Eqs. (12) and (13) into Eq. (9) gives

$$V(t) = \frac{V_0}{2} + \sum_{n=1}^{\infty} K_n \cos\left(n\omega t_0 + \frac{n\pi}{2}\right), \text{ for } t_0 = \frac{T}{2} \tag{14}$$

Figure 7 shows the equivalent circuit of the ferromagnetic toroid. The following admittance can be obtained:

$$Y = \frac{(R_\omega + jn\omega L) + \frac{1}{jn\omega C_\omega}}{(R_\omega + jn\omega L)\frac{1}{jn\omega C_\omega}}$$

$$= \frac{1}{R_\omega^2 + n^2\omega^2 L^2}\left[R_\omega + j\left(n\omega R_\omega^2 C_\omega - n\omega L + n^3\omega^3 L^2 C_\omega\right)\right] = |Y|\angle\theta_1 \tag{15}$$

$$I(jn\omega) = YV(t) = C_0 Y_0 + \sum_{n=1}^{\infty} 2K_n |Y| \cos(n\omega t + \angle C_n + \theta_1) \tag{16}$$

From Eq. (7), it can be shown that

$$V_{eff} = -\frac{1}{dt}\int_s \vec{B}\cdot d\vec{s} = -\frac{1}{dt}\left[\frac{\mu_0\mu NI(jn\omega)}{\mu_0(2\pi r_0 - l_g) + \mu l_g}\cdot\Delta zd\right] \tag{17}$$

$$= \frac{\mu_0\mu N(\Delta zd)}{\mu_0(2\pi r_0 - l_g) + \mu l_g}\sum_{n=1}^{\infty} 2K_n |Y| n\omega \sin(n\omega t + \angle C_n + \theta_1) \tag{18}$$

$$= \sum_{n=1}^{\infty} 2KK_n |Y| n\omega \sin(n\omega t + \angle C_n + \theta_1)$$

$$K = \frac{\mu_0 \mu N \Delta z d}{\mu_0 \left(2\pi r_0 - l_g \right) + \mu l_g} \tag{19}$$

Figure 8 shows the equivalent circuit of the experimental measurement system.

In Fig. 8, the V_{out} signal supplied to the oscilloscope and signal analyzer is given by

$$V_{out} = V_{eff} \frac{K_1}{R_S} \cdot \frac{K_3 \angle \theta_3}{K_2 \angle \theta_2} \cdot \frac{R_i}{K_4 \angle \theta_4} \tag{20}$$

where $K_1 = R_S // R_m \; R_m = 1/h_{oe} // \gamma_L$ for a small value of C_{ce}.

$$Q_2 = K_1 - j\frac{1}{\omega C} = K_2 \angle \theta_2 \tag{21}$$

$$K_2 = \left[K_1^2 + \left(\frac{1}{\omega C} \right)^2 \right]^{\frac{1}{2}}$$

$$\theta_2 = \tan^{-1} \frac{-\frac{1}{\omega C}}{K_1} \tag{22}$$

$$Q_3 = K_2 \angle \theta_2 // R_L = K_3 \angle \theta_3 = a + bj \tag{23}$$

$$K_3 = \frac{1}{\left(K_1 + R_2 \right)^2 + \left(\frac{1}{\omega C} \right)^2} \left\{ \left[K_1 R_L \left(K_1 + R_L \right) + \frac{R_2}{\omega^2 C^2} \right]^2 \right.$$

$$\left. + \left[\frac{K_1 R_L}{\omega C} - \left(K_1 + R_L \right) \frac{R_L}{\omega C} \right]^2 \right\}^{1/2}$$

$$\theta_3 = \tan^{-1} \frac{\frac{K_1 R_L}{\omega C} - \left(K_1 + R_L \right) \frac{R_L}{\omega C}}{K_1 R_L \left(K_1 + R_L \right) + \frac{R_L}{\omega^2 C^2}} \tag{24}$$

$$Q_4 = \left(R_m // R_S + X_C \right) // R_L + X_C + R_i = Q_3 + X_C + R_i$$

$$= a + R_i + j \left(b - \frac{1}{\omega C} \right) = K_4 \angle \theta_4 \tag{25}$$
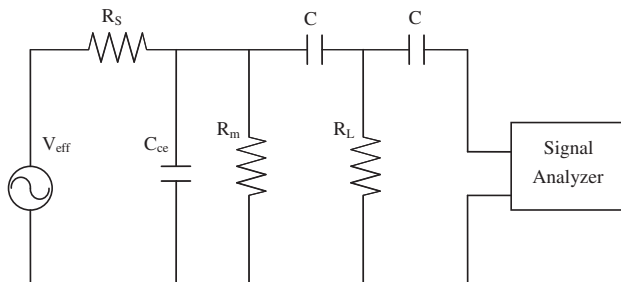

Figure 8. Equivalent circuit of experimental measurement system.

$$K_4 = \left[(a + R_i)^2 + \left(b - \frac{1}{\omega C} \right)^2 \right]^{\frac{1}{2}} \qquad (26)$$

$$\theta_4 = \tan^{-1} \frac{b - \frac{1}{\omega C}}{a + R_i} \qquad (27)$$

From the preceding equations, it can be shown that

$$V_{out} = \sum_{n=1}^{\infty} \frac{2KK_n |Y| n\omega K_1 K_3 R_i \sin(n\omega t + \angle C_n + \theta_1 + \theta_3 - \theta_2 - \theta_4)}{R_s K_2 K_4}$$

$$V_{out} = \sum_{n=1}^{\infty} \frac{C_3 2KK_n |Y| n\omega K_1 K_3 R_i}{R_s K_2 K_4} \sin(n\omega t + \angle C_n + \theta_1 + \theta_3 - \theta_2 - \theta_4) (28)$$

where the constant C_3 is the effective inducted coefficient. Equation (28) shows that the magnitude of the EMI-induced noise is governed by the pulse height, the output load, the parasitic capacitance, the interference frequency and the interference amplitude.

3.3. Noise Analysis

Conducting wires (CWs) render IC circuits highly susceptible to the effects of EMI and noise [17–24]. When a periodic square wave is applied across points A and B in Fig. 1, the CW in the air gap of the ferromagnetic torroid induces a pulse voltage in the RCPSO, which in turn produces a response noise spectrum. Fig. 9 shows the typical response wave for a periodic pulse with a period T. The periodic pulse function can be analyzed by taking the discrete Fourier transformation of function S_n, i.e.,

$$S_n = \frac{1}{T} \left[\int_{-T_0}^{0} -A_1 e^{-a(T_0 + t)} e^{-j\omega n t} dt + \int_0^{T_0} A_2 e^{-at} e^{-j\omega n t} dt \right]$$

$$= \frac{1}{T} \frac{a - j\omega n}{a^2 + \omega^2 n^2} [E - jD] \qquad (29)$$

where

$$E = A_1 e^{-aT_0} + A_2 - A_2 e^{-aT_0} \cos \omega n T_0 - A_1 \cos \omega n T_0 \qquad (30)$$

$$D = -A_2 e^{-aT_0} \sin \omega n T_0 + A_1 \sin \omega n T_0 \qquad (31)$$

$$S_n^2 = \frac{1}{T^2 (a^2 + \omega^2 n^2)} \left[E^2 + D^2 \right] \qquad (32)$$

in which n is an integer, $\omega = 2\pi f = 2\pi/T$, a is the attenuation factor of the exponential function, and A_1 and A_2 are the amplitudes of the
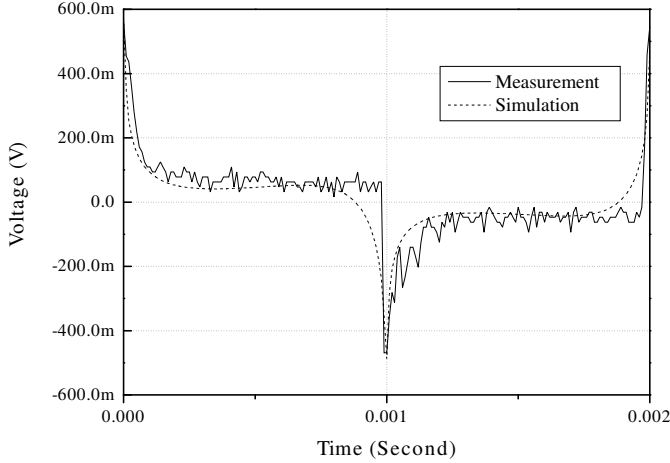
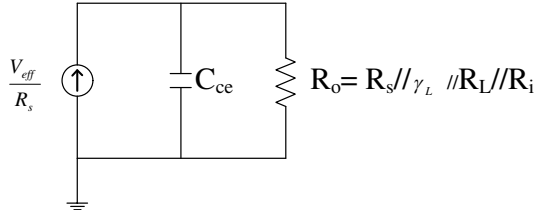**Figure 9.** Typical response wave of EMI noise induced in RCPSO.

Figure 10. Simplified representation of EMI output port in Fig. 8.

upper-half and lower-half periods of the EMI induced by the CW, respectively.

The amplitude spectrum of the EMI current can be obtained by plotting S_n against discrete frequencies, i.e., ω_n. The square of S_n has dimensions A^2 and corresponds to the current power spectrum $S_{i\lambda}(f_n)$ over $2T$ [25].

Regarding the parasitic capacitance of the RCPSO, the Norton equivalent output circuit is shown in Fig. 10. Let $V_{Cce} = V_C$ and $C_{ce} = C$. It therefore follows that

$$i_n = i_C + i_0 = C\frac{d\Delta V_C}{dt} + \frac{\Delta V_C}{R_0} \Rightarrow \frac{d\Delta V_C}{dt} + \frac{\Delta V_C}{R_0 C} = \frac{i_n}{C} \qquad (33)$$

where $R_0 = R_s//\gamma_L//R_L//R_i$ and ΔV_c is the variation of the voltage across the capacitor.

Taking the Fourier series expansions of ΔV_c and i_λ gives

$$\frac{i_n}{C} = \frac{1}{C} \sum_{n=-\infty}^{\infty} \alpha_n \exp(j\omega_n t) \tag{34}$$

$$\frac{d(\Delta V_{cn})}{dt} + \frac{\Delta V_{cn}}{R_0 C} = \frac{1}{C} \alpha_n \exp(j\omega_n t) \tag{35}$$

It can therefore be shown that

$$\Delta V_{cn} = \beta_n \exp(j\omega_n t) \tag{36}$$

where

$$\beta_n = \frac{\alpha_n R_0}{1 + j\omega_n R_0 C} \tag{37}$$

Therefore, the noise power spectrum $S_{\Delta Vc}(f_n)$ of the RCPSO is given by

$$S_{\Delta Vc}(f_n) = 2T\overline{\beta_n \beta_n^*} \tag{38}$$

$$S_{\Delta Vc}(f_n) = S_{i\lambda}(f_n)\frac{R_0^2}{1 + (\omega_1 n R_0 C)^2} \tag{39}$$

where

$$S_{i\lambda}(f_n) = 2T\overline{\alpha_n \alpha_n^*} = 2T S_n^2 \tag{40}$$
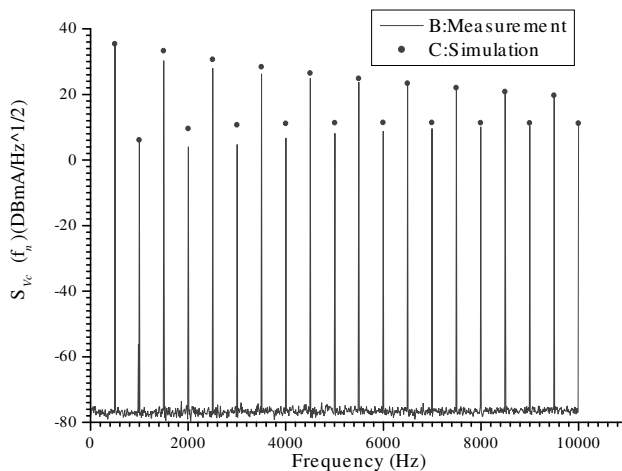

Figure 11. Harmonic wave component of RCPSO noise spectrum response for $V_P = 0.6\,\text{V}$ and $f = 500\,\text{Hz}$. (Note that in obtaining the simulation results using Eq. (41), A_1 and A_2 are specified as $24855\,\mu\text{A}$ and $24847\,\mu\text{A}$, respectively).

From Eqs. (32), (39) and (40), it can be shown that

$$S_{\Delta V_C}(f_n) = 2T \frac{R_0^2}{1 + (\omega_1 n R_0 C)^2} \left[\frac{1}{T^2(a^2 + \omega^2 n^2)}(E^2 + D^2) \right] \quad (41)$$

The total noise power induced in the RCPSO can be obtained by summing $S_{\Delta Vc}(f_n)$ over all possible integers, n. In identifying the relative magnitudes of the various harmonic components within the power spectrum, the present analysis first finds the value of A (the pulse height) from the measured power spectral intensity of the fundamental harmonic and then evaluates the power spectral intensities of the higher-order harmonics. Adopting this approach, the typical experimental response wave shown in Fig. 9 can be transformed into the noise spectrum shown in Fig. 11 and the value of the EMI then quantified directly.

3.4. Effects of Basic Output Frequency of RCPSO on Output Power

The basic output frequency of a RCPSO has the form of a sine wave. Generally speaking, the effects of the basic output frequency on the noise power spectrum of an oscillator can be mitigated using an impedance-matching method. Fig. 12(a) shows the output equivalent circuit of the EMI signal supplied to the oscilloscope and signal analyzer, where $R_{O1} = 1/h_{oe}//R_C//R_{L1}//R_L//R_i = 41.60\,\Omega$. Meanwhile, Fig. 12(b) shows the equivalent circuit of the RCPSO sine wave output signal, where $R_{O2} = 1/h_{oe}//R_S//R_{L1}//R_L//R_i = 23.23\,\Omega$. The output powers of the EMI and oscillator signals can be
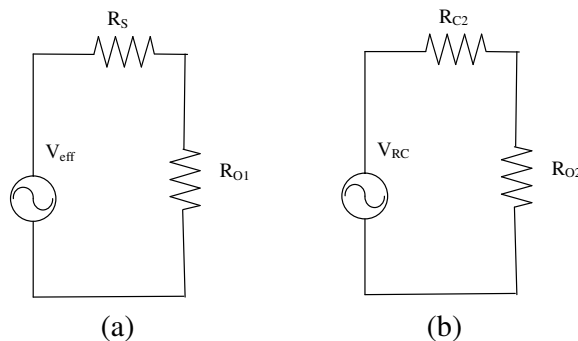

(a)   (b)

Figure 12. Output equivalent circuits of (a) EMI signal and (b) RCPSO signal.

obtained respectively as

$$P_{EMI} = \left(\frac{V_{eff}}{50 + 41.60}\right)^2 41.60 = 0.00496(V_{eff})^2 \tag{42}$$

$$P_{RC} = \left(\frac{V_{RC}}{1^k + 23.23}\right)^2 23.23 = 2.219 \times 10^{-5}(V_{RC})^2 \tag{43}$$

From Eqs. (42) and (43), $P_{RC}/P_{EMI} = 0.00447$. In other words, the output power of the RCPSO is negligible compared to that of the EMI-induced signal and can therefore be neglected.

4. RESULTS AND DISCUSSION

Figure 9 presents the experimental and simulation results for the typical periodic pulse function generated in the RCPSO by a periodic EMI signal with a period T. Note that in obtaining the simulation results using Eq. (28), the following parameter values are assumed: $V_0 = 0.58\,\text{V}$ (at time $t = 0$), $V_0 = 0.48\,\text{V}$ (at time $t = T/2$), $\mu_0 = 4\pi E - 7\,\text{H/m}$, $\mu_r = 4000$, $N = 500$, $F = 500\,\text{Hz}$, $R_\omega = 0.52\,\Omega$, $r_0 = 0.09\,\text{m}$, $l_g = 0.005\,\text{m}$, $C_\omega = 6.558E - 10F$, $1/h_{oe} = 30\,\text{k}\Omega$, $R_C = 1\,\text{k}\Omega$, $R_1 = R_2 = R_3 = 1\,\text{k}\Omega$, $C = 100E - 6F$, $\Delta z = 0.01\,\text{m}$, $d = 0.001\,\text{m}$, $R_s = 50\,\Omega$, $C_3 = 0.083$, $X_C = 1/(2\pi fC)$, $R_L = 220\,\text{k}\Omega$, $L = 1E - 4H$, $\omega = 2\pi f$ and $R_i = 50\,\Omega$. Figure 9 confirms that a good agreement exists between the simulated pulse function and the
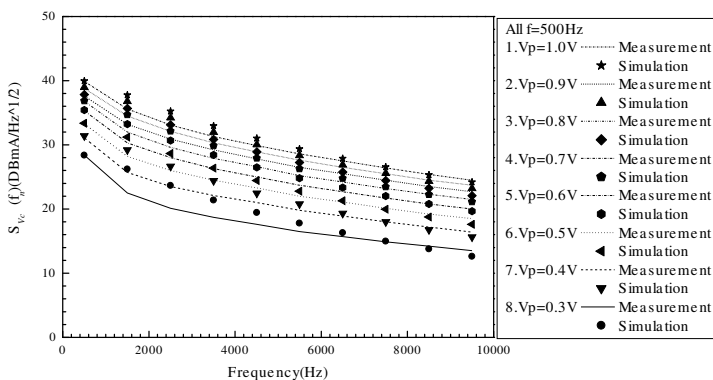

Figure 13. Experimental and simulation results for odd-order harmonics of noise spectrum induced in RCPSO by EMI interference with frequency of $500\,\text{Hz}$ and amplitude of $V_p = 0.3 \sim 1.0\,\text{V}$. (Note that the simulation results computed using Eq. (41) are shown using filled symbols).

experimental function. In the experimental setup shown in Fig. 1, $C_{ce} = 12.77E - 8F$, $R_L = 220\,\text{k}\Omega$, and $T_0 = 0.4942T$. Utilizing a value of $a = 10622$ in Eq. (41), Fig. 11 compares the experimental and simulation results for the harmonic wave component of the noise spectrum induced in the RCPSO by EMI with an amplitude of $V_P = 0.6\,\text{V}$ and a frequency of $f = 500\,\text{Hz}$. Again, a good agreement is observed between the two sets of results. To further investigate the effect of EMI on the noise spectrum induced in the RCPSO, the amplitude of the AC interference signal was varied between $0.3\,\text{V}$ and $1.0\,\text{V}$ while the frequency was maintained at a constant $f = 500\,\text{Hz}$. Fig. 13 presents the experimental and simulation results for the odd-order harmonics of the resulting noise spectrum. Note that in obtaining the simulation results using Eq. (41), A_1 ranges from $11057 \sim 41856\,\mu\text{A}$ while A_2 ranges from $11047 \sim 41845\,\mu\text{A}$. It is observed that a good agreement is obtained between the experimental and simulation results for all values of V_p.

Table 1 compares the measured and simulated peak values of the harmonic components of the maximum noise power spectral intensity for EMI with amplitudes in the range of $V_P = 0.3 \sim 1.0\,\text{V}$ and a constant frequency of $f = 500\,\text{Hz}$. (In other words, the harmonic value varies only as a function of the interference amplitude while the remaining parameters are constant.) Table 2 compares the experimental and simulation results for the maximum noise power spectral intensity for EMI frequencies in the range of $300\,\text{Hz} \sim 1\,\text{kHz}$ and constant interference amplitudes of $A_1 = 21455\,\mu\text{A}$ and $A_2 = 21447\,\mu\text{A}$. (In other words, the noise power spectral intensity varies only as a function of the AC interference frequency while the other parameters remain constant). Fig. 14 presents the experimental and simulation results for the odd-order harmonics of the noise spectrum

Table 1. Comparison of experimental and theoretical results for maximum noise power spectral intensity of RCPSO for various values of V_p.

Frequency fixed, Amplitude variable (First harmonic wave)								
V_p (V)	0.3	0.4	0.5	0.6	0.7	0.8	0.9	1.0
Frequency (Hz)	500	500	500	500	500	500	500	500
Measurement (dBmA/Hz$^{1/2}$)	28.4	31.1	33.3	35.3	36.8	37.6	38.8	39.9
Simulation (dBmA/Hz$^{1/2}$)	28.6	31.5	33.4	35.4	36.8	37.8	38.9	39.9

Table 2. Comparison of experimental and theoretical results for maximum noise power spectral intensity of RCPSO for various values of frequency.

Amplitude fixed, Frequency variable (First harmonic wave)								
Frequency (Hz)	300	400	500	600	700	800	900	1000
Measurement (dBmA/Hz$^{1/2}$)	31.2	32.7	34	34.6	35.6	35.9	36.3	36.6
Simulation (dBmA/Hz$^{1/2}$)	32.2	33.3	34.2	34.8	35.3	35.7	36	36.3

Figure 14. Experimental and simulation results for odd-order harmonics of noise spectrum induced in RCPSO by EMI interference frequency of $300 \sim 700\,\mathrm{Hz}$ and amplitude of $V_p = 0.5\,\mathrm{V}$. (Note that the simulation results computed using Eq. (41) are shown using filled symbols).

induced in the RCPSO by EMI interference with a frequency of $300 \sim 700\,\mathrm{Hz}$ and an amplitude of $V_p = 0.5\,\mathrm{V}$. Although a $-2\,\mathrm{dB}$ difference is observed between the two sets of results, it is clear that the EMI frequency has a significant effect on the noise response of the RCPSO. By tuning the amplitude parameters in recognition of the fact that a variable EMI frequency affects both the attenuation factor and the induced wave type, the same degree of simulation accuracy as that shown in Fig. 13 can be obtained (see Fig. 15 and Table 3). In other words, the EMI frequency is a function of the EMI amplitude, as proven in Eqs. (28) and (41).

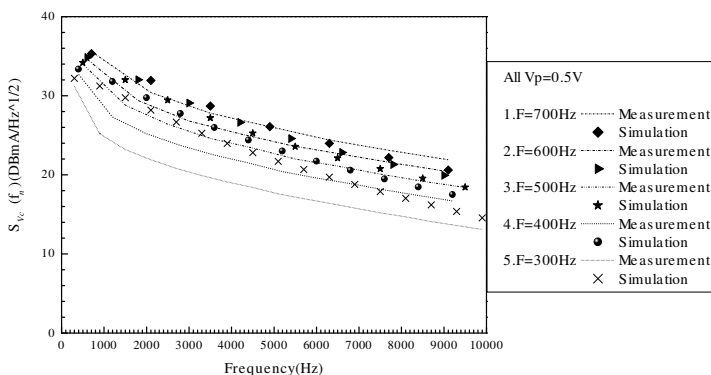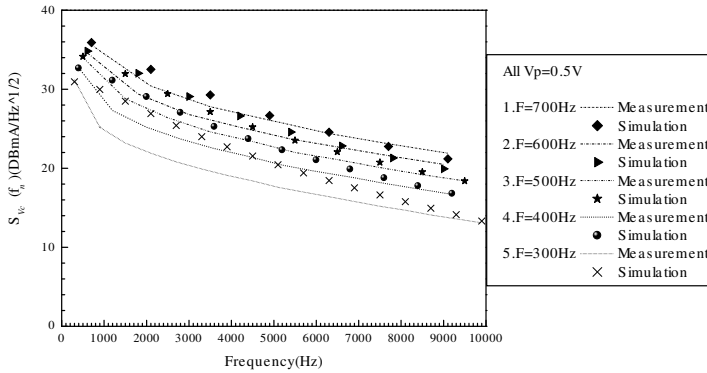Although Fig. 14 shows that the frequency has a significant effect

Figure 15. Experimental and simulation results for odd-order harmonics of noise spectrum induced in RCPSO by EMI interference frequency of $300 \sim 700\,\mathrm{Hz}$ and variable amplitude parameters A_1 and A_2 (see Table 3). (Note that the simulation results computed using Eq. (41) are shown using filled symbols).

Table 3. Comparison of experimental and theoretical results for maximum noise power spectral intensity of RCPSO for various values of frequency and amplitude.

Amplitude, Frequency variable (First harmonic wave)					
Frequency (Hz)	300	400	500	600	700
Induced Current $A_1(\mu\mathrm{A})$	18656	19954	21455	21554	23056
Induced Current $A_2\ (\mu\mathrm{A})$	18648	19946	21447	21548	23045
Measurement $(\mathrm{dBmA/Hz^{1/2}})$	31.2	32.7	34	34.6	35.6
Simulation $(\mathrm{dBmA/Hz^{1/2}})$	30.9	32.7	34.1	34.8	35.9

on the odd-order harmonic waves (i.e., Eq. (41) denotes $d\omega/dA_1 \neq 0$ and $d\omega/dA_2 \neq 0$ for the nonlinear function $S_{\Delta Vc}(f_n)$), Fig. 13 shows that the difference between the experimental and simulation results for the variable amplitude case is less than that for the variable frequency case. In other words, the amplitude of the EMI has a greater effect on the noise response of the RCPSO than the frequency. In practice, this implies that the parasitic capacitance and dynamic input resistance of

Table 4. Relative SNR of current induced by EMI.

V_P (V)	1.0	0.9	0.8	0.7	0.6	0.5	0.4	0.3
Induced Current A_1 (µA)	41856	37354	32855	29356	24855	19654	15653	11057
Induced Current A_2(µA)	41845	37346	32848	29348	24847	19646	15648	11047
Induced Peak Current N_i (µA)	8.37	7.47	6.57	5.87	4.97	3.93	3.13	2.21
Relative SNR (dBµA)	1.545*	2.534*	3.649*	4.627*	6.073*	8.112*	10.089*	13.112*

*Where SNR $= 20\log(S_i/N_i)$, $S_i = 10\,\mu\text{A}$, $N_i = ((A_1 + A_2)/2)/5000$ and $f = 500\,\text{Hz}$.

the RCPSO vary with a varying frequency.

In general, the simulation and experimental results presented above indicate that the magnitude of the EMI induced by the CW is affected by the amplitude, frequency and period of the interference signal, the drain resistance and parasitic capacitance of the RCPSO, the output load, and parameter a. Table 4 summarizes the relative signal-to-noise (SNR) ratio of the oscillator for interference amplitudes in the range of $V_P = 0.3 \sim 1.0\,\text{V}$, a constant frequency of $f = 500\,\text{Hz}$ and a reference signal of $S_i = 10\,\mu\text{A}$.

The CW used in the present EMI experiments has a length of 1 cm. Thus, if the CW in a practical electrical circuit has a length of 1 m (say), the EMI effects will potentially be magnified 100 times compared to those observed in the present study. For example, assuming an induced current of 4.97 µA, a CW of length 1 cm, and a load resistance of 45 Ω, the induced voltage is 223 µV. This value may potentially be amplified by up to 1000 times in a practical amplified system; resulting in a significant EMI effect. According to CISPR 11 (published by the International Special Committee on Radio Interference), EMI should be limited to no more than 110 dBµV in the interference frequency range of $0.009 \sim 0.050\,\text{MHz}$, equivalent to a voltage of 316227 µV. As a result, a general design guideline of no more than 1.42 cm is obtained for the maximum length of the CW in an RCPSO.

5. CONCLUSION

Experimental and theoretical methods have been used to characterize the noise spectrum of an RCPSO subject to periodic EMI induced via a CW. A good agreement has been observed between the experimental and simulation results for the noise spectral intensity of the RCPSO in both the time domain and the frequency domain. In general, the results have shown that the noise response of the oscillator is significantly affected by EMI. Specifically, the degree of the EMI effect on the RCPSO is determined by the radiated power of the interference source and the following circuit parameters: f, V_0, μ_0, μ_r, N, R_ω, r_0, l_g, R_s, R_C, R_1, R_2, R_3, C_ω, C_{ce}, R_i, Δ_z, d, L, A_1, A_2, a, T_0, R_L and C. Furthermore, it has been shown that the magnitude of the induced interference current increases with an increasing interference frequency and an increasing interference amplitude. Of these two factors, the amplitude of the EMI has a greater effect on the noise response of the oscillator than the frequency. In accordance with CISPR and EN norms, the results presented in this study suggest that the length of the CWs used in practical RCPSOs should not exceed 1.42 cm. Whilst the methods outlined in this study have focused specifically on the case of RCPSOs, they are equally applicable to the EMI analysis of all general wavelength-based electronic devices.

ACKNOWLEDGMENT

REFERENCES

1. Hung, F. S., F. Y. Hung, and C. M. Chiang, "Crystallization and annealing effects of sputtered tin alloy films on electromagnetic interference shielding," *Applied Surface Science*, Vol. 257, 3733–3738, 2011.

2. Hu, C. N. and H. C. Ko, "Improved IC production yield by taking into account the electromagnetic interference level during testing," *IEEE Transactions on Electromagnetic Compatibility*, Vol. 53, No. 2, 266–273, 2011.

3. Mustafa, F. and A. M. Hashim, "Properties of electromagnetic fields and effective permittivity excited by drifting plasma waves in semiconductor-insulator interface structure and equivalent transmission line technique for multi-layered structure," *Progress In Electromagnetics Research*, Vol. 104, 403–425, 2010.

4. Mustafa, F. and A. M. Hashim, "Generalized 3D transverse magnetic mode method for analysis of interaction between drifting plasma waves in 2 deg-structured semiconductors and electromagnetic space harmonic waves," *Progress In Electromagnetics Research*, Vol. 102, 315–335, 2010.

5. Tsai, H.-C., "Investigation into time- and frequency-domain EMI-induced noise in bistable multivibrator," *Progress In Electromagnetics Research*, Vol. 100, 327–349, 2010.

6. Yang, T., Y. Bayram, and J. L. Volakis, "Hybrid analysis of electromagnetic interference effects on microwave active circuits within cavity enclosures," *IEEE Transactions on Electromagnetic Compatibility*, Vol. 52, No. 3, 745–748, 2010.

7. Khah, S. K., T. Chakravarty, and P. Balamurali, "Analysis of an electromagnetically coupled microstrip ring antenna using an extended feedline," *Journal of Electromagnetic Waves and Applications*, Vol. 23, No. 2–3, 369–376, 2009.

8. Hong, J.-I., S.-M. Hwang, and C.-S. Huh, "Susceptibility of microcontroller devices due to coupling effects under narrow-band high power electromagnetic waves by magnetron," *Journal of Electromagnetic Waves and Applications*, Vol. 22, No. 17–18, 2451–2462, 2009.

9. Dlugosz, T. and H. Trzaska, "A new calibration method for non-stationary electromagnetic fields measurements," *Journal of Electromagnetic Waves and Applications*, Vol. 23, No. 17–18, 2471–2480, 2009.

10. Heydari, H., V. Abbasi, and F. Faghihi, "Impact of switching-induced electromagnetic interference on low-voltage cables in substations," *IEEE Transactions on Electromagnetic Compatibility*, Vol. 51, No. 4, 937–944, 2009.

11. Toh, T. C., "Electromagnetic interference laboratory correlation study and margin determination," *IEEE Transactions on Electromagnetic Compatibility*, Vol. 51, No. 2, 204–209, 2009.

12. Tsai, H. C. and K. C. Wang, "Investigation of EMI-induced noise spectrum on an enhancement-type MOSFET," *Solid State Electronics*, Vol. 52, No. 8, 1207–1216, 2008.

13. Kim, Y. J., U. Choi, and Y. S. Kim, "Screen filter design considerations for plasma display panels (PDP) to achieve a high brightness with a minimal loss of EMI shielding effectiveness," *Journal of Electromagnetic Waves and Applications*, Vol. 22, No. 5–6, 775–786, 2008.

14. Tsai, H. C., "Numerical and experimental analysis of EMI effects on circuits with MESFET devices," *Microelectronics Reliability*,

Vol. 48, No. 4, 537–546, 2008.

15. Tsai, H. C., "An investigation on the influence of electromagnetic interference induced in conducting wire of universal LEDs," *Microelectronics Reliability*, Vol. 47, No. 6, 959–966, 2007.

16. Cheng, D. K., *Field and Wave Electromagnetics*, 2nd Edition, 252–634, Addison-Wesley Publishing Company, USA, 1989.

17. Yan, L., F.-L. Yang, and C.-L. Fu, "A new numerical method for the inverse source problem from a Bayesian perspective," *International Journal for Numerical Methods in Engineering*, Vol. 85, No. 11, 1460–1474, 2011.

18. Lee, H. S., Y. H. Hong, and H. W. Park, "Design of an FIR filter for the displacement reconstruction using measured acceleration in low-frequency dominant structures," *International Journal for Numerical Methods in Engineering*, Vol. 82, No. 4, 403–434, 2010.

19. Tsai, H.-C. and K.-C. Wang, "Simulated and experimental analysis of surface state and $1/f^r$ noise on GaAs MESFET devices," *Japanese Journal of Applied Physics*, Vol. 48, No. 7, 071101-1–8, 2009.

20. Bhatia, V. and B. Mulgrew, "Non-parametric likelihood based channel estimator for Gaussian mixture noise," *Signal Processing*, Vol. 87, No. 11, 2569–2586, 2007.

21. Chambers, J., D. Bullock, Y. Kahana, A. Kots, and A. Palmer, "Developments in active noise control sound systems for magnetic resonance imaging," *Applied Acoustics*, Vol. 68, No. 3, 281–295, 2007.

22. Roelant, R., D. Constales, G. S. Yablonsky, R. van Keer, M. A. Rude, and G. B. Marin, "Noise in temporal analysis of products (TAP) pulse responses," *Catalysis Today*, Vol. 121, No. 3–4, 269–281, 2007.

23. Lisnanski, R. and J. A. Weiss, "Low complexity generalized EM algorithm for blind channel estimation and data detection in optical communication systems," *Signal Processing*, Vol. 86, No. 11, 3393–3403, 2006.

24. Li, H. G. and G. Meng, "Detection of harmonic signals from chaotic interference by empirical mode decomposition," *Chaos, Solitons and Fractals*, Vol. 30, No. 4, 930–935, 2006.

25. Van der Ziel, A., *Noise in Solid State Devices and Circuits*, 10–20, Wiley, New York, 1986.